Atmos. Chem. Phys. Discuss., doi:10.5194/acp-2015-964, 2016
Manuscript under review for journal Atmos. Chem. Phys.
Published: 19 January 2016

Atmospheric Chemistry and Physics Discussions

The Importance of Plume Rise on the Concentrations and Atmospheric Impacts of Biomass Burning Aerosol

Carolin Walter[1], Saulo R. Freitas[2], Christoph Kottmeier[1], Isabel Kraut[1], Daniel Rieger[1], Heike Vogel[1], and Bernhard Vogel[1]

[1]Karlsruhe Institute of Technology, Institute for Meteorology and Climate Research, Karlsruhe, Germany
[2]CPTEC Center for Weather Forecasts and Climate Studies, National Institute for Space Research, Cachoeira Paulista, Brazil

Correspondence to: Carolin Walter (carolin.walter@kit.edu)

Abstract. We quantified the effects of the plume rise of biomass burning aerosol and gases for the forest fires that occurred in Saskatchewan, Canada, in July 2010. For this purpose, simulations with different assumptions regarding the plume rise and the vertical distribution of the emissions were conducted. Based on comparisons with observations, applying a one-dimensional plume rise model to predict the injection layer in combination with a parametrisation of the vertical distribution of the emissions outperforms approaches in which the plume heights are initially predefined. Approximately 30 % of the fires exceed the height of 2 km and the maximum height is 8.6 km. Using this plume rise model, comparisons with satellite images in the visible spectral range show a very good agreement between the simulated and observed spatial distributions of the biomass burning plume. The simulated AOD with data of an AERONET station is in good agreement with respect to the absolute values and the timing of the maximum. Comparison of the vertical distribution of the biomass burning aerosol with CALIPSO retrievals also showed the best agreement when the plume rise model was applied. We found that down-welling surface short-wave radiation below the forest fire plume is reduced by up to 50 % and that the 2 m temperature is decreased by up to 6 K. In addition, we simulated a strong change in atmospheric stability within the biomass burning plume.

1 Introduction

Emissions from biomass burning significantly contribute to the global atmospheric aerosol mass (Stocker et al., 2013). A total aerosol particle mass of 1.33 Tg of vegetation is burned each year, which implies a release of 12.7 Gg of particles with diameters of less than 2.5 μm (Zhang et al., 2012). Biomass burning aerosol degrades air quality (Ignotti et al., 2010), impacts aviation by reducing visibility, modifies the radiative fluxes and has an impact on cloud micro-physics and precipitation. Therefore, there is an urgent need to forecast the dispersion of biomass burning aerosol and its impact on the state of the atmosphere on the time scale of days. This is currently not performed in the majority of operational forecast centres (i.e., weather services), with few exceptions, such as the Brazilian center CPTEC/INPE, which has been running operationally since 2003 (Freitas et al., 2005). However, note that quantifying the effects of biomass burning aerosol on cloud formation and precipitation is still an unresolved scientific problem.

Atmos. Chem. Phys. Discuss., doi:10.5194/acp-2015-964, 2016
Manuscript under review for journal Atmos. Chem. Phys.
Published: 19 January 2016

Atmospheric Chemistry and Physics Discussions

In the summer of 2002, the U.S. east coast experienced some of the worst air quality days during the passage of biomass burning plumes (Colarco et al., 2004). The emissions were released into the air over central Quebec, Canada, and further transported with a descending air mass prior to being mixed into the boundary layer of Washington D.C., USA. Another example of extreme air pollution is the Russian wildfires in 2010, which caused a very high aerosol concentration in the Moscow region and dramatically reduced visibility (Konovalov et al., 2011). During the summer of 2010, the Russian fires emitted approximately 10 Tg of CO, which is more than 85 % of the annual anthropogenic CO emissions in this region. In their study, they developed an optimisation procedure to quantify the wildfire emissions. As a result, their simulated concentrations of CO and PM10 were well correlated with the measured concentrations.

The radiative impact of biomass burning aerosol depends on the size distribution and optical properties of the particles. Fires emit gaseous precursors of aerosol and primary particles such as soot. The optical properties of soot produced by different fuels were investigated by Colbeck et al. (1997). Flaming combustion at high temperatures was found to produce smoke, which strongly absorbs solar radiation. Smouldering combustion at lower temperatures produces aerosol that predominantly scatters light. Incomplete combustion leads to smoke particles that contain a substantial fraction of unburned organic matter. The presence of more elemental carbon leads to blacker smoke. Furthermore, the ageing of the particles leads to a change in chemical composition and a shift in the size distribution due to coagulation processes, which influence the radiative properties (Sakamoto et al., 2015). Local heating due to the absorption of radiation results in the evaporation of cloud droplets and in the dissolution of clouds. This is called the semi-direct aerosol effect (Lohmann and Feichter, 2001). Depending on their size distribution and chemical composition, the aerosol particles can also act as cloud condensation nuclei or as ice nuclei. Consequently, aerosol particles might change cloud properties such as albedo, lifetime and precipitation efficiency.

Koren et al. (2004) utilised MODIS data to analyse cloud cover under smoky conditions. The stable meteorological conditions and homogeneous cloud distribution in the Amazon without the presence of smoke provided an ideal basis for investigating the impact of biomass burning aerosol on cloud formation. They determined a mean cloud cover reduction of 50 % for an Aerosol Optical Depth (AOD) of 0.6. An increase in the AOD led to a further reduction in cloud cover. When the AOD increased above 1.3, no more clouds were present. Biomass burning aerosol is also known to have an influence on precipitation and to cause hail events, which are not reported for smoke-free conditions (Ding et al., 2013; Andreae et al., 2004).

Ding et al. (2013) explicitly investigated the influence of extreme air pollution due to biomass burning on weather forecasting. A temperature of 34 °C was predicted for Nanjing, China, for 10 June 2012, but the temperature only reached 26.5 °C. The high concentration of scattering and absorbing aerosol reduced the solar radiation by 70 %. This influence of high pollution conditions on weather is justified by the fact that under unpolluted conditions on the previous days, the model forecast agreed well with observations. During such events, the forecast quality of numerical models was dramatically decreased because scattering and absorbing biomass burning particles were not considered.

In the case of forest fires, not only is the total emitted mass of importance but high amounts of energy are also released into the atmosphere. Thus, the buoyancy of the plume becomes important for the injection height. Due to the heat released by the fires and the temperature difference between the plume and the environment, an updraft is initiated that transports the emitted gases and aerosols to higher altitudes. The height at which the emissions are effectively released is critical for a reliable

Atmos. Chem. Phys. Discuss., doi:10.5194/acp-2015-964, 2016
Manuscript under review for journal Atmos. Chem. Phys.
Published: 19 January 2016

Atmospheric Chemistry and Physics Discussions

simulation of the transport of the emitted chemical species. In the free atmosphere, aerosol has a considerably longer lifetime. Moreover, the aerosol is quickly transported out of the source region by the prevailing wind. The effective source height defines the height below which the emitted material is released in a model system to represent the real plume. The effective source height depends on the heat released by the fire and on the environmental conditions: temperature, stability, humidity and wind speed (Penner et al., 1986). Additional buoyancy can be gained through the release of latent heat by condensation, whereas a strong horizontal wind prevents the air parcel from reaching the condensation level (Freitas et al., 2007).

Observations show that smoke plumes of biomass burnings commonly reach the free troposphere or even exceed it and penetrate the stratosphere (Andreae et al., 2004; Trentmann et al., 2006). In some cases, pollutants originating from Canadian forest fires have even been detected over Europe (Fiebig et al., 2003; Waibel et al., 1999). In the standard version of GEOS-Chem (Goddard Earth Observing System with Chemistry), pyrogenic emissions are released at the model surface (Mu et al., 2011). Assuming that the emissions are dispersed within the boundary layer is only sufficient for small fires (Tosca et al., 2011). A common method in aerosol transport modelling is to assume a vertically homogeneous distribution of the fire emissions from the ground to a certain height (Wang et al., 2006). For example, Pfister et al. (2005) utilised a vertically homogeneous distribution between the surface and 400 hPa for simulations in Alaska. Wang et al. (2013) simulated the transport of smoke from fires over the South-east Asian Maritime Continent for September and October 2006. They concluded that in comparison with CALIOP (Cloud-Aerosol Lidar with Orthogonal Polarisation) observations, simulations with homogeneous emissions between the surface and 800 m provided the best agreement for the aerosol profile. Another simulation with homogeneous emissions between the surface and 2 km showed a rather different picture than the CALIOP profile. The same effective source height was used by Ge et al. (2014). However, observations with the Multi-angle Imaging SpectroRadiometer (MISR) on-board the NASA Terra satellite showed that with sufficient buoyancy, the aerosol is not distributed homogeneously up to a certain height (Kahn et al., 2007; Val Martin et al., 2010). Moreover, the aerosol is concentrated in a discrete, elevated layer of relative stability after being transported through the boundary layer by the initial buoyancy. According to observations by Kahn et al. (2007), this layer is located between 5 and 6.5 km. Aerosol also concentrates at 1 km when originating from sources with less initial buoyancy. Smoke layers in a stable stratified atmosphere are not as deep as layers in an unstable stratified atmosphere (Val Martin et al., 2010). Val Martin et al. (2010) indicated that both the fire intensity and the stability of the atmosphere are crucial for the effective source height.

Including a one-dimensional, subgrid-scale plume rise model in an existing chemistry and transportation model has the potential to enhance the representation of fire emissions in model simulations (Freitas et al., 2007; Sessions et al., 2011). The one-dimensional model calculates the upper and lower bounds of the injection layer depending on meteorological conditions, fire size and fire intensity for every fire location. The emitted material is released between these bounds (Freitas et al., 2007). Sessions et al. (2011) simulated the source height with the one-dimensional plume rise model implemented in WRF-Chem (Weather Research and Forecast modeling system coupled with chemistry). The source heights of the plume rise model are in good agreement with satellite-retrieved source heights. The model results are compared with basic distributions such as injection in the boundary layer and injection in the layer between 3-5 km. The conclusion is that different source heights lead to different transportation paths.

Atmos. Chem. Phys. Discuss., doi:10.5194/acp-2015-964, 2016
Manuscript under review for journal Atmos. Chem. Phys.
Published: 19 January 2016

Atmospheric Chemistry and Physics Discussions

Sofiev et al. (2012) use Convective Available Potential Energy (CAPE) calculations to constrain plume heights. In this method dynamical entrainment is neglected. The plume height depends on stratification, turbulent entrainment, fire size and heat release. The function for the plume height is fitted to MISR fire observations.

Another possibility to account for the fire-induced buoyancy in the determination of the effective source height is to decrease the grid spacing, thereby allowing the buoyancy-driven dynamics and the resulting convective plumes to be explicitly solved by the model. Trentmann et al. (2002) simulated a fire experiment in Quinault (Washington, USA) in 1994 using the Active Tracer High-resolution Model (ATHAM). The model domain had a size of 35x28 km^2 and a vertical extension of 3.75 km, with a minimum horizontal grid spacing of 50 m and in vertical 20 m at the centre. This model was also applied for simulating the pyroconvection of the Chisholm fire in Alberta, Canada, in 2001 (Luderer et al., 2006; Trentmann et al., 2006). This fire was a strong event with emissions that were transported up to the stratosphere.

In this study, we extend the comprehensive online-coupled model system COSMO-ART (Vogel et al., 2009) to quantify the influence of biomass burning aerosol on the state of the atmosphere. To account for the fire-induced buoyancy of fire emissions, we incorporate the one-dimensional plume rise model of Freitas et al. (2006). We use the daily GFASv1.1 (Global Fire Assimilation System) datasets for the fire emissions. A parametrisation of the diurnal cycle for fires in boreal forests is developed. With this framework, we are able to consider chemical processes such as particle formation and the photochemical ageing of the released particles. As a case study, we simulate a fire event that occurred in July 2010 in the north of Saskatchewan, Canada. Several simulations with different setups are conducted to evaluate the importance of plume height on the smoke distribution. Furthermore, we investigate the radiative impact of the biomass burning aerosol.

In section 2, a short description of COSMO-ART is presented. Then, the one-dimensional plume rise model is explained. The results of a sensitivity study are presented to motivate the coupling of a plume rise model with a comprehensive model system. The emission database is described, and the optical properties of the emissions are discussed. In section 3, the simulation results are presented and evaluated. A comparison with observations is given, and the impacts of the biomass burning emissions on radiation and temperature are presented.

2 Model description

The simulations are conducted using the comprehensive online coupled model system COSMO-ART (Consortium for Small-scale Modelling - Aerosols and Reactive Trace gases) (Vogel et al., 2009). This system is based on the operational weather forecast model COSMO (Baldauf et al., 2011). COSMO-ART includes a comprehensive chemistry module to describe the gaseous composition of the atmosphere and secondary aerosol formation, and it allows for feedback of the simulated aerosol particles with radiation, cloud formation, and precipitation (Stanelle et al., 2010; Knote et al., 2011; Bangert et al., 2012; Lundgren et al., 2013; Athanasopoulou et al., 2014; Rieger et al., 2014; Vogel et al., 2014). The size distribution of aerosol within COSMO-ART is approximated by overlapping log-normal distributions. In Table 1, all required modes with their initial median diameters, standard deviations and chemical compositions are presented. The standard deviation is maintained constant.

Atmos. Chem. Phys. Discuss., doi:10.5194/acp-2015-964, 2016
Manuscript under review for journal Atmos. Chem. Phys.
Published: 19 January 2016

Atmospheric Chemistry and Physics Discussions

2.1 Plume rise model

The model system COSMO-ART is extended by the one-dimensional, sub-grid-scale plume rise model of Freitas et al. (2006, 2007, 2010), which is briefly summarised in the following. The plume rise model accounts for buoyancy, atmospheric stratification, and flow conditions to calculate the plume height. The relevant processes occur on a considerably smaller scale than the grid size of regional modelling systems such as COSMO-ART. The one-dimensional plume rise model uses a grid spacing of 100 m with 200 vertical layers. The environmental conditions, such as pressure, humidity, temperature and wind speed, are calculated by COSMO-ART. Hourly, for every grid point with an active fire, the values of these variables are transferred to the plume rise model. Within an hour, the input variables are maintained constant. The parameters fire size and fire intensity depending on vegetation type and density have to be set. With these variables, the heat release and the initial buoyancy are calculated. The lower boundary condition is based on the assumption of a virtual source of buoyancy below the surface, resulting in a high vertical velocity at the surface. The final buoyancy is limited by turbulent and dynamic entrainment. Turbulent entrainment leads to dilution and an increased plume radius. The latter accounts for the environmental wind speed and the possibility of a bent-over of the smoke plume. The buoyancy is increased by latent heat release when condensation occurs. By definition, the top of the plume is reached as soon as the vertical velocity decreases below $1\ \mathrm{m\,s^{-1}}$. To achieve upper and lower bounds of the effective emission layer, two values are chosen for the parameter fire intensity. This is a robust approach for obtaining a vertical extended layer with the advantage that the environmental conditions control the extension. For the upper bound, we specified 80 $\mathrm{kWm^{-2}}$. For the lower bound, the value is 30 $\mathrm{kWm^{-2}}$. The fire area is set to 50 ha. In this way, we obtain a buoyancy-dependent thickness of our layer.

To demonstrate the importance of meteorological conditions on the maximum height of the plume top, a sensitivity study was performed. This was done for a fixed fire size and a fire intensity of 80 $\mathrm{kWm^{-2}}$ for an imaginary fire in central Saskatchewan. The results are summarised in Fig. 1. We prescribed the profile of the potential temperature (Fig. 1a) and the horizontal wind speed (Fig. 1b) for 16 and 17 July 2010 at 18:00 UTC as the environmental conditions. The buoyancy calculated by the plume rise model for these conditions is depicted in (Fig. 1c), and the resulting vertical velocity is shown in (Fig. 1d). The top of the plume on 16 July 2010 is reached at an altitude of 5300 m. The next day, the plume does not exceed 2200 m. The horizontal wind speed on 17 July is at least twice as high as that on 16 July, leading to a strong dynamical entrainment that decreases the buoyancy. The potential temperature indicates a stable stratification for 16 July. On 17 July, the stratification is strongly unstable at the surface and is becoming more neutral up to 1200 m. Thus, the initial buoyancy is considerably greater in this case. The buoyancy decreases very strongly with increasing horizontal wind speed, but the plume arises out of the unstable layer because of its inertia. Although the buoyancy on 16 July has a smaller initial value and reaches its minimum at lower altitude, the resulting maximum plume height is greater. This result is due to the additional buoyancy gained by latent heat release from condensation starting at an altitude of approximately 1200 m on this day. This single example already shows the substantial impact of meteorological conditions on plume rise.

Atmos. Chem. Phys. Discuss., doi:10.5194/acp-2015-964, 2016
Manuscript under review for journal Atmos. Chem. Phys.
Published: 19 January 2016

Atmospheric Chemistry and Physics Discussions

2.2 Vertical distribution of the emissions

The emissions are distributed with a parabolic function defined between the upper and the lower bounds, according to the following expression:

$$f(z^*) = 6 \cdot z^* \cdot (1 - z^*)\,. \tag{1}$$

The dimensionless height z^* is determined by

$$z^* = \frac{z - z_{bot}}{z_{top} - z_{bot}}, \tag{2}$$

where z is the model layer height and z_{top} and z_{bot} are the cloud tops determined by the plume rise model using the upper and lower limits for the heat flux, describing the upper and lower bounds of the emission layer. Consequently, we obtain $0 \leq z^* \leq 1$. Implying a given total emission Q_{tot}, the emission profile can be calculated depending on z^*:

$$Q(z^*) = \begin{cases} Q_{tot} \cdot f(z^*) & \text{if } 0 < z^* < 1 \\ 0 & \text{else.} \end{cases} \tag{3}$$

To obtain the portion of the total emissions that is released in the respective grid cell, the parabolic function is integrated from the lower level of the grid cell (z^*_{lolev}) to the upper level of the grid cell (z^*_{uplev}):

$$\int_{z^*_{lolev}}^{z^*_{uplev}} f(z^*)dz^* = \left[3z^{*2} - 2z^{*3}\right]_{z^*_{lolev}}^{z^*_{uplev}}. \tag{4}$$

2.3 Diurnal cycle

The intensity of vegetation fires depends on the time of day. This dependency is subject to the diurnal cycle of meteorological variables such as temperature, humidity and wind speed. For ignition, the humidity of the biomass load has to be 35 % or less. During daytime, the humidity at the surface is reduced due to solar irradiation and increasing turbulent mixture, therefore, ignition and fire spread are favoured. The spread is also advanced due to a higher wind speed (McRae et al., 2005). The wind speed in the boundary layer is higher during daytime than at night. Accordingly, fires have a diurnal cycle with maximum emissions in the early afternoon and minimum emissions at night (Prins et al., 1998). Wang et al. (2006) claimed that the application of hourly emission data is crucial for a realistic dispersion of the smoke near the source region. With geostationary satellites, it is possible to characterise the diurnal cycle of the fires (Kaiser et al., 2009b). Zhang and Kondragunta (2008) analysed the daily variability by considering variations of the fire pixel size. The diurnal cycle is not only a function of meteorological conditions but also dependent on the vegetation type of the burning biomass (Giglio, 2007). According to

Atmos. Chem. Phys. Discuss., doi:10.5194/acp-2015-964, 2016
Manuscript under review for journal Atmos. Chem. Phys.
Published: 19 January 2016

Atmospheric Chemistry and Physics Discussions

Zhang and Kondragunta (2008), the daily maximum of the fire pixel size is reached between 1000 and 1500 local solar time (LST). During this period, 52.1 % of the daily amount of emissions are released in a forest. In the off-peak time, the hourly emissions are 2-4 % of the daily amount. A diurnal cycle may be specified through a weighted normal distribution (Kaiser et al., 2009a).

$$d(t_l) = w + (1-w)\frac{24h}{\sigma\sqrt{2\pi}} exp\left(-\frac{1}{2}\left(\frac{t_l - t_0}{\sigma}\right)^2\right) \quad (5)$$

where w is the weighting, t_l denotes the local solar time, t_0 is the expected value, and σ is the standard deviation. We designate the values as $w = 0.3$, $t_0 = 12.5\ h$ and $\sigma = 2.5\ h$. Subsequently, the equation expresses the diurnal cycle for forest fires as described by Zhang and Kondragunta (2008), and it is shown in Fig. 2. This diurnal cycle is overlaid on the mean values of fire size and fire intensity used in the plume rise calculation.

2.4 Radiative properties

The influence of aerosol on radiative transfer is determined by its composition and size distribution. To perform simulations with aerosol-radiation interactions with COSMO-ART, the optical properties of the aerosol have to be determined. The optical properties were obtained through Mie calculations. For these calculations, the refractive index of a constituent must be given. Because COSMO-ART was primarily developed to investigate pollutants from industry and traffic, the refractive index of diesel soot was used to calculate the optical properties for the soot portion in aerosol particles (Riemer et al., 2003). The optical properties are namely the specific extinction coefficient, the specific single-scattering albedo and the specific asymmetry parameter. These specific values for every constituent are then multiplied by the mass fraction of the constituent. The coefficients also depend on wavelength. The specific extinction coefficient for soot in COSMO-ART should be in sufficient agreement. A value of 9.0 $\mathrm{m}^2\ \mathrm{g}^{-1}$ for the spectral range of 0.25 to 0.7 μm is used, while laser measurements at a wavelength of 0.632 μm suggest a value of 7.8 $\mathrm{m}^2\ \mathrm{g}^{-1}$ for soot originating from wood (Colbeck et al., 1997). The AOD is determined from this coefficient. The single-scattering albedo characterises the particle absorption. It is given by the ratio of the specific scattering coefficient to specific extinction coefficient; thus, values towards zero characterise strongly absorbing particles, and a value of one represents non-absorbing particles. Colbeck et al. (1997) investigated soot produced by different fuels. Measurements of the single-scattering albedo yielded a value of 0.30 for diesel and a value of 0.62 for wood at a wavelength of 0.632 μm. In COSMO-ART, the single-scattering albedo is set to 0.1834 for the spectral range of 0.25 to 0.7 μm. This implies that soot from biomass burning must be less absorbing than diesel soot. However, we were unable to perform new Mie calculations in this study. Using the optical properties of diesel soot for our simulations, we may slightly overestimate the absorption in layers of dense smoke.

Atmos. Chem. Phys. Discuss., doi:10.5194/acp-2015-964, 2016
Manuscript under review for journal Atmos. Chem. Phys.
Published: 19 January 2016

Atmospheric Chemistry and Physics Discussions

3 Case study

Our simulations are performed for the wildfires that occurred in 2010 in the north of Saskatchewan, Canada. Boreal fires frequently occur following warm and dry periods when the moisture content of the fuel is lowered. A change in the synoptic situation in connection with lightnings and freshening wind often leads to a violent fire condition (Johnson, 1995).

3.1 Model configuration

For the fire emissions, a dataset provided by the Global Fire Assimilation System (GFAS v1.1) is used. It is a satellite-retrieved dataset based on daily Fire Radiative Power (FRP) measurements by MODIS on-board the polar orbiting satellites Aqua and Terra. FRP is a quantity that specifies the amount of thermal radiation released by a fire. It is proportional to fuel consumption and emission production (Wooster et al., 2005). Global emission fields for a comprehensive list of species are derived from these FRP observations (Kaiser et al., 2009a). Because GFAS uses daily averaged FRP, the retrieved emission rates are also daily products, without any information about diurnal variations. We used 31 gaseous and particulate species derived from GFASv.1.1, which are allocated into the existing substance classes in COSMO-ART.

The simulations were started at 6:00 UTC 10 July 2010, i.e., midnight at local time. The simulations were conducted for 10 days with a horizontal grid spacing of 7 km. The simulation domain is shown in Fig. 3. The fires indicated by the red dots for 15 July 2010 occurred mainly in the north of Saskatchewan. We used 40 vertical non-equidistant layers, and the top of the model domain is at an altitude of approximately 20 km. The integration time step was 25 seconds. For meteorological initial and boundary conditions, the output of the global model GME is employed (Majewski et al., 2002). The initial and boundary concentrations of trace gases are derived from MOZART-4/GEOS (Wiedinmyer et al., 2011). Biogenic emissions are calculated online within the model system. Furthermore, sea salt emissions are considered because the Hudson Bay is located in the model domain. Anthropogenic emissions are neglected because the model domain is sparsely populated. However, the province Alberta, located in the western part of the model domain, has oil sand extraction facilities. In comparison with biomass burning emissions, this industry causes only a minor contribution to the aerosol load and is assumed to have no significant influence (Howell et al., 2014).

3.2 Simulations

Five different simulations were performed to assess the benefit of a plume rise model. For the simulation VARHEIGHT, COSMO-ART is applied in combination with the plume rise model mentioned in the previous sections. The parameters fire area and fire intensity have a diurnal cycle according to equation 5. The emission source strength is maintained constant within 24 hours. The simulation EMISSCYCLE is the same, except the emission source strength also has a diurnal cycle. Thus, the emission strength is proportional to the fire size and fire intensity. This means that during night when the fire size and fire intensity are small and the emissions are frequently released at ground level, the emission strength is also low. The simulations 800M and 7500M have the same daily mean emission source strength as VARHEIGHT. However, the emissions are vertically homogeneously distributed from the surface to 800 m and 7500 m, respectively. These distributions are chosen according to

Atmos. Chem. Phys. Discuss., doi:10.5194/acp-2015-964, 2016
Manuscript under review for journal Atmos. Chem. Phys.
Published: 19 January 2016

Atmospheric Chemistry and Physics Discussions

Wang et al. (2013) and Pfister et al. (2005), respectively. For the simulation NOFIRE, no biomass burning emissions were considered. All simulations are itemised in Table 2.

3.3 Plume heights

Kahn et al. (2007) used MISR data to quantify the physical characteristics of biomass burning plumes. They showed that the biomass burning plumes frequently reach heights well above the planetary boundary layer (PBL) depending on atmospheric stratification. Emissions reaching heights well above the boundary layer encounter reduced vertical mixing. This can lead to well-defined and long-lasting shallow aerosol layers. In this case, it can no longer be assumed that the aerosol above a location of the fire is vertically well mixed. Gonzi et al. (2015) applied a one-dimensional plume rise model in global-scale GEOS-Chem simulations during the year 2006. They concluded that approximately 80 % of the injections of biomass burning aerosol occur below the boundary layer height. Fig. 6 shows the simulated frequency distribution of the simulated plume heights based on the ten-day period of our situation. Approximately 50 % of the plume heights are below 1 km. At least 30 % of the plume heights are above 2 km and are therefore above the PBL. This percentage represents a lower limit because the PBL height is expected to be quite frequently below 2 km. Ten percent of the plumes are reaching more than 3 km, and the simulated maximum plume height is 8.6 km.

3.4 Comparison with observations

To verify our simulation results and to assess the importance of using a one-dimensional plume rise model, the simulations are compared with different remote sensing products. The satellite image (Fig. 4, left) shows the smoke distribution on 15 July 2010 at 17:55 UTC. The image is in the visible spectral range and was derived by MODIS on-board Terra. The smoke distribution pattern develops in several stages. First, the emissions of the fires are affected by a northern flow from the trough on 11 July 2010 (Fig. 5, left). During the next days, a low-pressure system passes the model domain from west to east, and it is located in the south-west of the model domain on 14 July (Fig. 5, right). In the west of the model domain, the next through is approaching. The low-pressure system affects the southern fires and transports the smoke to the south. The northern fires are affected by the trough and the corresponding front. Thus, these emissions are transported northwards, and after reaching 64° N, they are bent to the east. The model output of AOD at 550 nm in Fig. 4 on the right is in good agreement with the observed complex smoke structure, e.g., for run VARHEIGHT, which performs the best as outlined later. AOD is between 0.1 and 0.5 in areas not affected by smoke. In parts of the dense smoke plume, a maximum of 4 is reached. The comparison shows that the meteorological conditions and the transport processes are well captured with COSMO-ART.

To compare the simulated heights of the smoke layers with observations, retrievals of CALIOP are used. CALIOP on-board the polar orbiting CALIPSO (Cloud-Aerosol Lidar and Infrared Pathfinder Satellite Observation) satellite retrieves vertical profiles of clouds and aerosol along its track (CALIPSO Science Team, 2015). The aerosol products are provided in a horizontal resolution of 5 km x 5 km and 60 m in the vertical direction. The detected aerosol is classified into aerosol subtypes. These different subtypes, namely, clean marine, dust, polluted continental, clean continental, polluted dust, and smoke, are determined with an associated aerosol lidar ratio at 532 nm and 1064 nm (Omar et al., 2009). The confidence in aerosol subtyping can be

Atmos. Chem. Phys. Discuss., doi:10.5194/acp-2015-964, 2016
Manuscript under review for journal Atmos. Chem. Phys.
Published: 19 January 2016

Atmospheric Chemistry and Physics Discussions

reduced by thick cloud layers. Furthermore, dense dust and smoke near their source are likely to be misclassified (Liu et al., 2009).

The overpass of CALIPSO at approximately 9:20 UTC on 16 July 2010 is indicated by the purple line in Fig. 3. In Fig. 7a, the CALIOP aerosol retrievals are shown. At the northernmost edge at approximately 64° N, polluted continental aerosol is detected at a height between 6.75 and 9.5 km. Smoke is detected between 63 and 62° N at an altitude from 6 to 7.5 km. Between 62 and 59° N, the satellite identified smoke, polluted dust and polluted continental aerosol within the lowest 3.5 km. From 56 to 54° N, columns with different heights consisting of smoke, polluted dust, clean continental and polluted continental aerosol are found. Starting at 54° N, a layer of smoke descending from 5 km down to 3 km at 51° N and further down to 1.5 km at 50° N is observed. Another smoke layer is located between 52 and 51° N at an altitude between 1 and 2 km. Among these smoke regions, polluted dust and, underneath some smoke regions, polluted continental aerosol were detected. The presence of clouds over wide parts of the satellite track lowers the quality of CALIOP aerosol identification. The signal is attenuated. Because aerosol subtypes are pre-defined by distinct values for the extinction-to-backscatter ratio, this could mismatch the actual aerosol type. A cross-section along the satellite track is conducted for each of the simulations. Smoke is defined to be present when the soot concentration is greater than 0.01 $\mu g\ m^{-3}$. Simulation 800M is unable to simulate the elevated smoke at 62° N (Fig. 7b). It only simulates smoke up to 3 km at this location. At 60° N, where CALIOP found the smoke top at 3.5 km, 800M produces the top at 2.5 km. The northern smoke region starts at 59° N in all simulations, as also observed by CALIOP. In simulation 800M, the southern smoke region starts at 54.5° N at the ground, followed by a layer of smoke within the lowest 2 km. A descending layer starts at 53.5° N and at a height of 4.5 km. At 52° N, the top is at 3 km, and in the very south of the shown track, it descends to 1.5 km. The smoke in simulation 7500M starts in the north with a top at 9.5 km (Fig. 7c). This is the position of the polluted continental aerosol detected by CALIOP. At 62° N, where CALIOP detects the smoke top at 7.5 km, the simulation underestimates the top by 0.5 km, which is approximately the vertical grid spacing at this height. At 61° N, the top fits the observations; however, at 59° N, the top is simulated at 2.5 km, which underestimates the observation by 1 km. The southern part of the descending layer starts at 56° N, which is the most north of all simulations. The top height is 10 km or even greater. The layer descends to 1.5 km in the southern edge. At 52° N, the top is at 3 km, as observed. The smoke layer underneath begins at 54.5° N and has an overall top at approximately 1.5 km. In the simulation VARHEIGHT (Fig. 7d), the observed polluted continental aerosol at 64° N is represented with a plume top at 8 km. At approximately 62° N, the plume top is located at approximately 7 km, the same as in the simulation 7500M and at 500 m less than observed. Between 61.5° N and 59° N, the smoke layer has a height of 3 km and 2.5 km. Further in the south, the first smoke is present at 55° N at the surface and becomes a thicker layer towards the south with a height of 2 km. Above this layer, a descending smoke layer starts at 53.5° N at an altitude of 5.5 km, reaching 3.5 km at 52° N and decreasing to 1.5 km at 50° N. The simulation EMISSCYCLE (Fig. 7e) shows a smoke top at 10 km or above at the northern edge at 64° N. At 62° N, the plume reaches 7.5 km, which is consistent with the CALIPSO observation. Between 62 and 60.5° N, the smoke top is higher than 5 km. Between 60 and 59° N, the top is located at approximately 2 km, whereas CALIOP detected smoke columns with a height of 3.5 km in this region. The descending smoke layer in the south starts at 54° N according to the satellite measurements, but starting at an

Atmos. Chem. Phys. Discuss., doi:10.5194/acp-2015-964, 2016
Manuscript under review for journal Atmos. Chem. Phys.
Published: 19 January 2016

altitude of 6 km, it is 1 km higher than observed. As in all other simulations, the layer descends towards an altitude of 1.5 km at 50° N. The horizontal layer underneath has a height of 2 km.

In summary, we found that the simulated smoke distribution depends strongly on the source emission height. For the various scenarios, the occurrence of smoke is very different. When the emission height is restricted to 800 m, the vertical development of the plume is suppressed. Emissions released up to an altitude of 7500 m lead to a further mixing at higher layers, suggesting an unstable stratification at this altitude. Overall, the simulation VARHEIGHT performs best and is the simulation used in our further investigations to represent the fire case.

To further evaluate the individual simulations, we use the AERONET database. An AERONET station is located in the south of our simulation domain. The station Bratts Lake (Fig. 3) provides level 2.0 data for July 2010. In Fig. 8, the AOD is displayed for 15 July 2010 (UTC). The black line denotes the AERONET sun photometer measurements. During night time and under cloudy conditions, no observations are performed. Between 12:00 and 16:00 UTC, the measured AOD reaches 0.6. After a short drop at 16:00 UTC, the AOD increases to 1.1 at 18:00 UTC. The simulation VARHEIGHT agrees very well with the measurements between 12:00 and 15:00 UTC but does not decrease at 16:00 UTC; rather, it reaches the same maximum value one hour earlier. The AOD in the simulation 800M increases to 1.15 at 17:00 and 18:00 UTC. The simulation EMISSCYCLE has its maximum AOD at 16:00 UTC with a value of 1.4. The simulation 7500M does not have that great of a peak; the curve is flat with its maximum of approximately 0.9 at 14:00 UTC. The simulations EMISSCYCLE and VARHEIGHT also show a local maximum at 8:00 UTC with an AOD of 1.2 and 0.9, respectively. In general, COSMO-ART represents the measured AOD well. The best fit is obtained with the simulation VARHEIGHT. The time of the peak of AOD is well captured, even though the transport path is quite long.

In the next section, we show the importance of considering aerosol for numerical weather predictions.

3.5 Aerosol radiative impact

The light absorbing and scattering processes of aerosol with exceptionally high concentrations are not considered in most numerical weather prediction models. Instead, an aerosol climatology is used. This leads to erroneous forecasts for temperature and radiation during such events. However, the increasing fraction of solar energy production in many countries requires accurate forecasts of the expected photovoltaic power.

The simulated effect of biomass burning aerosol on radiation is influenced by the optical properties of the aerosol, which depend on the size distribution and the chemical composition. The characterisation of the optical properties of aerosol in COSMO-ART was discussed in section 2.4. The simulated mean number and mass size distribution for a small domain in dense smoke near Fort Smith (Fig. 3) at 18:00 UTC on 15 July 2010 are shown in Fig. 9. This figure shows the mean over all grid points where more than 400 soot-containing particles per cm^3 are present. The black line denotes pure soot, and the red line denotes the sum of all modes. Pure soot has a number median diameter of approximately 0.01 μm. The mean median particle diameter is 0.1 μm. Regarding the mass size distribution, the mean median diameter is greater than 1 μm. Unfortunately, we have no in situ characterisation of the aerosol particles. Therefore, we compare our model results with observations of previous studies. Sakamoto et al. (2015) specifies the size distribution by a number-median diameter of 0.23 μm and a standard deviation

Atmos. Chem. Phys. Discuss., doi:10.5194/acp-2015-964, 2016
Manuscript under review for journal Atmos. Chem. Phys.
Published: 19 January 2016

Atmospheric Chemistry and Physics Discussions

of 1.7. The values were measured in 1-2-day-old smoke during a campaign in East Canada in 2011. They performed simulations to provide suggestions for the size distribution of fresh emissions. For different entrainment scenarios, they obtained median diameters between 0.059 and 0.094 μm. In small-scale laboratory experiments, the range was measured to be 0.029-0.052 μm for different plant types (Hosseini et al., 2010). Therefore, we can conclude that the diameter of our simulated aerosol is somewhat smaller than the observed diameter.

In Fig. 10, the difference between considering and neglecting biomass burning aerosol in surface short-wave radiation is presented. The figure shows the model results from the simulation VARHEIGHT for the location of Fort Smith, which is heavily influenced by smoke, for five days starting on 11 July 2010. On the first day, Fort Smith is not influenced by smoke. Surface short-wave radiation is the same in both scenarios. On 12 July 2010, small differences are simulated, which are mostly caused by changes in cloud cover. The cloud cover is influenced by the biomass burning aerosol; thus, the differences occur in both directions. On the one hand, the availability of aerosol could lead to condensation on these particles and cloud formation; on the other hand, absorbing aerosol could lead to warming and dissolution of clouds. On 13 and 14 July 2010, the surface short-wave radiation reaches approximately 660 W m^{-2} at noon (LT) when the fires are not considered. With biomass burning aerosol, the surface short-wave radiation only reaches a maximum value of approximately 340 W m^{-2}. This means a reduction of up to 50 % due to smoke. On 15 July 2010, a strong decrease also exists, but clouds are also present. The biomass burning aerosol leads to a shift in cloud cover. Consequently, the surface short-wave radiation increases during specific periods. Bergstrom et al. (2003) calculated a surface radiative forcing of -208 W m^{-2} for Mongu, Zambia, on 6 September 2000 due to biomass burning haze. This again shows that our results are reasonable.

Changes in the surface short-wave downward radiation have an impact on the temperature at a height of 2 m. This impact is quantified in Fig. 11 for the entire model domain at 18:00 UTC on 15 July 2012. The temperature reduction is strongest for areas in the north and south of the Great Slave Lake in the north-western part of the model domain. The temperature is reduced by up to 6 K. Most of the areas where a high AOD is simulated in Fig. 4 now belong to a cooling region, with an exception adjacent to the fire location. In the east and in the south-east of Lake Athabasca, there is an increase in the 2 m temperature, which is caused by changes in cloud patterns. Thus, the smoke can have a cooling and a warming effect on the 2 m temperature. In the remaining model domain, many small areas with a temperature increase alternate with areas with a temperature reduction. The reason for this result is changes in cloud cover due to modified atmospheric flow patterns caused by biomass burning aerosol and perturbed clouds. An even higher temperature difference due to vegetation fires is reported by Ding et al. (2013). During a biomass burning situation in East China, 7.5 K are in between the forecast and the observations.

The influence of biomass burning aerosol on the vertical temperature profile is shown in Fig. 12. This figure shows the mean vertical temperature difference between the simulations VARHEIGHT and NOFIRE for a small area around Fort Smith at 18:00 UTC on 15 July 2010. At this time and location, the soot is distributed between the surface and a height of 4 km. The fire aerosol leads to a temperature decrease of up to 4 K at the surface. At a height of approximately 1 km, the sign changes due to an increase in temperature with a maximum of 1 K at a height of 2 km. At approximately 4.5 km, clearly above the soot layer, the temperature is decreased again, alternating slightly with height up to 15 km. The soot layer absorbs the incoming radiation, leading to a local warming. Less radiation is able to reach the lower levels near the ground, which leads

Atmos. Chem. Phys. Discuss., doi:10.5194/acp-2015-964, 2016
Manuscript under review for journal Atmos. Chem. Phys.
Published: 19 January 2016

Atmospheric Chemistry and Physics Discussions

to a temperature reduction in comparison with a smoke-free atmosphere. Temperature changes in various atmospheric layers affect the atmospheric stratification. An increase in static atmospheric stratification is found in such cases. This is in good agreement with Tummon et al. (2010), who found in their climate simulations a decrease in surface turbulent fluxes, a reduced PBL height and reduced surface temperatures. Radiative absorption by biomass burning aerosol resulted in diabatic warming of the atmosphere of up to 1 K near 700 hPa. Surface cooling and heating at altitude stabilised the lower troposphere below 700 hPa. Above this, stability was found to be reduced.

Fig. 13 illustrates the height sensitivity of radiation forecasts on the parametrisation of the plume height and the vertical distribution of the emissions. The various simulations show a very different course of the incoming short-wave radiation for all four days with smoke influence. The altitude and the distribution of the smoke release do not refer to a certain magnitude of reduction. For example, in the afternoon of 13 July 2010, the simulation 800M yields approximately 520 W m^{-2} and simulation VARHEIGHT only 280 W m^{-2}. On the next day, the incoming radiation simulated by 800M is always slightly smaller than that simulated by VARHEIGHT. This implies again the necessity of a correct plume height treatment.

4 Conclusions

We extended the model system COSMO-ART with an online coupled one-dimensional plume rise model to parametrise the effective source heights for vegetation fires with high energy input. Furthermore, a function to parametrise the diurnal cycle of boreal fires is proposed and included. The improved model system was used to quantify the effects of biomass burning aerosol on radiation and temperature during an intensive fire event that occurred in July 2010 in Canada. Simple parametrisations of the effective source height were compared to the results obtained using the plume rise model. The utilised optical properties and the achieved aerosol size distribution are consistent with the literature. Comparisons with satellite observations showed that COSMO-ART is able to represent the spatial distribution of the smoke. The simulated AODs with the different assumptions of the effective source height are compared with the observed AODs of the AERONET station Bratts Lake. The simulation where the one-dimensional plume rise model was used together with the diurnal cycle on fire size and intensity match best in magnitude and timing. Including the diurnal cycle of the emissions did not lead to further improvements in our results. This shows that further improvement of the diurnal cycle is required. The vertical extension of the smoke plume was evaluated through a comparison with CALIPSO retrievals. A fixed effective plume height of 7500 m completely overestimates the top of the smoke layer. For the fixed plume height of 800 m, the initial height is frequently exceeded, but elevated smoke layers are not represented. The simulations using the plume rise model performed better. Approximately 50 % of the fire plumes remained in the lowermost 1 km and 30 % of the simulated plumes exceeded a height of 2 km. The fire emissions caused a reduction in surface short-wave downward radiation of up to 50 % under cloudless conditions. The radiation was absorbed in dense smoke layers. The 2 m temperature below these layers decreased by up to 6 K, whereas the temperature in the smoke layer was increased. The temperature change in the column affects the atmospheric stratification. Surface cooling and a warming in elevated layers lead to an increase in atmospheric stability.

Atmos. Chem. Phys. Discuss., doi:10.5194/acp-2015-964, 2016
Manuscript under review for journal Atmos. Chem. Phys.
Published: 19 January 2016

Acknowledgements. Thanks to I. Abboud and V. Fioletov for their effort in establishing and maintaining the AERONET site Bratts Lake.

Thanks to J. Kaiser and S. Remy at ECMWF for providing the GFASv1.1 data set.

We acknowledge the use of Rapid Response imagery from the Land Atmosphere Near-real time Capability for EOS (LANCE) system operated by the NASA/GSFC/Earth Science Data and Information System (ESDIS) with funding provided by NASA/HQ.

The CALIPSO data were obtained from the NASA Langley Research Center Atmospheric Science Data Center.

Atmos. Chem. Phys. Discuss., doi:10.5194/acp-2015-964, 2016
Manuscript under review for journal Atmos. Chem. Phys.
Published: 19 January 2016

Atmospheric Chemistry and Physics Discussions

References

Andreae, M. O., D. Rosenfeld, P. Artaxo, A. A. Costa, G. P. Frank, K. M. Longo, and M. A. F. Silva-Dias, 2004: Smoking rain clouds over the Amazon. *Science*, **303 (5662)**, 1337–1342, doi:10.1126/science.1092779.

Athanasopoulou, E., et al., 2014: Fire risk, atmospheric chemistry and radiative forcing assessment of wildfires in eastern Mediterranean. *Atmos. Environ.*, **95**, 113–125, doi:10.1016/j.atmosenv.2014.05.077.

Baldauf, M., A. Seifert, J. Förstner, D. Majewski, M. Raschendorfer, and T. Reinhardt, 2011: Operational convective-scale numerical weather prediction with the COSMO model: description and sensitivities. *Mon. Weather Rev.*, **139 (12)**, 3887–3905, doi:10.1175/MWR-D-10-05013.1.

Bangert, M., et al., 2012: Saharan dust event impacts on cloud formation and radiation over Western Europe. *Atmos. Chem. Phys.*, **12 (9)**, 4045–4063, doi:10.5194/acp-12-4045-2012.

Bergstrom, R. W., P. Pilewskie, B. Schmid, and P. B. Russell, 2003: Estimates of the spectral aerosol single scattering albedo and aerosol radiative effects during SAFARI 2000. *J. Geophys. Res.-Atmos.*, **108 (D13)**, doi:10.1029/2002JD002435, 8474.

CALIPSO Science Team, 2015: CALIPSO/CALIOP Level 2, Vertical Feature Mask Data, version 3.01, Hampton, VA, USA: NASA Atmospheric Science Data Center (ASDC), Accessed 21 November 2014. doi:10.5067/CALIOP/CALIPSO/CAL_LID_ L2_VFM-ValStage1-V3-01_L2-003.01.

Colarco, P., M. Schoeberl, B. Doddridge, L. Marufu, O. Torres, and E. Welton, 2004: Transport of smoke from Canadian forest fires to the surface near Washington, DC: Injection height, entrainment, and optical properties. *J. Geophys. Res.-Atmos.*, **109 (D6)**, doi:10.1029/2003JD004248, d06203.

Colbeck, I., B. Atkinson, and Y. Johar, 1997: The morphology and optical properties of soot produced by different fuels. *J. Atmos. Sci.*, **28 (5)**, 715–723, doi:10.1016/S0021-8502(96)00466-1.

Ding, A., et al., 2013: Intense atmospheric pollution modifies weather: a case of mixed biomass burning with fossil fuel combustion pollution in eastern China. *Atmos. Chem. Phys.*, **13 (20)**, 10 545–10 554, doi:10.5194/acp-13-10545-2013.

Fiebig, M., A. Stohl, M. Wendisch, S. Eckhardt, and A. Petzold, 2003: Dependence of solar radiative forcing of forest fire aerosol on ageing and state of mixture. *Atmos. Chem. Phys.*, **3 (3)**, 881–891, doi:10.5194/acp-3-881-2003.

Freitas, S., et al., 2007: Including the sub-grid scale plume rise of vegetation fires in low resolution atmospheric transport models. *Atmos. Chem. Phys.*, **7 (13)**, 3385–3398, doi:10.5194/acp-7-3385-2007.

Freitas, S. R., K. M. Longo, and M. O. Andreae, 2006: Impact of including the plume rise of vegetation fires in numerical simulations of associated atomospheric pollutants. *Geophys. Res. Lett.*, **33 (17)**, doi:10.1029/2006GL026608, l17808.

Freitas, S. R., K. M. Longo, J. Trentmann, and D. Latham, 2010: Technical Note: Sensitivity of 1-D smoke plume rise models to the inclusion of environmental wind drag. *Atmos. Chem. Phys.*, **10 (2)**, 585–594, doi:10.5194/acp-10-585-2010.

Freitas, S. R., et al., 2005: Monitoring the transport of biomass burning emissions in south america. *Environ. Fluid Mech.*, **5 (1-2)**, 135–167, doi:10.1007/s10652-005-0243-7.

Ge, C., J. Wang, and J. Reid, 2014: Mesoscale modeling of smoke transport over the Southeast Asian Maritime Continent: coupling of smoke direct radiative effect below and above the low-level clouds. *Atmos. Chem. Phys.*, **14 (1)**, 159–174, doi:10.5194/acp-14-159-2014.

Giglio, L., 2007: Characterization of the tropical diurnal fire cycle using VIRS and MODIS observations. *Remote Sens. Environ.*, **108 (4)**, 407–421, doi:10.1016/j.rse.2006.11.018.

Gonzi, S., P. I. Palmer, R. Paugam, M. Wooster, and M. N. Deeter, 2015: Quantifying pyroconvective injection heights using observations of fire energy: sensitivity of spaceborne observations of carbon monoxide. *Atmos. Chem. Phys.*, **15 (8)**, 4339–4355, doi:10.5194/acp-15-4339-2015, http://www.atmos-chem-phys.net/15/4339/2015/.

Hosseini, S., et al., 2010: Particle size distributions from laboratory-scale biomass fires using fast response instruments. *Atmos. Chem. Phys.*, **10 (16)**, 8065–8076, doi:10.5194/acp-10-8065-2010.

Howell, S., A. Clarke, S. Freitag, C. McNaughton, V. Kapustin, V. Brekovskikh, J.-L. Jimenez, and M. Cubison, 2014: An airborne assessment of atmospheric particulate emissions from the processing of athabasca oil sands. *Atmos. Chem. Phys.*, **14 (10)**, 5073–5087, doi:10.5194/acp-14-5073-2014.

Ignotti, E., S. S. Hacon, W. L. Junger, D. Mourão, K. Longo, S. Freitas, P. Artaxo, and A. C. Ponce de Leon, 2010: Air pollution and hospital admissions for respiratory diseases in the subequatorial Amazon: A time series approach. *Cad. Saúde Pública*, **26**, 747 – 761.

Johnson, E. A., 1995: Fire and vegetation dynamics: studies from the North American boreal forest. *Cambridge Univ. Pr.*

Kahn, R. A., W. H. Li, C. Moroney, D. J. Diner, J. V. Martonchik, and E. Fishbein, 2007: Aerosol source plume physical characteristics from space-based multiangle imaging. *J. Geophys. Res.-Atmos.*, **112 (D11)**, doi:10.1029/2006JD007647, d11205.

Kaiser, J. W., J. Flemming, M. G. Schultz, M. Suttie, and M. J. Wooster, 2009a: The MACC Global Fire Assimialtion System: First Emission Products (GFASv0). *Tech. Memo. 596, ECMWF, Reading*.

Kaiser, J. W., M. Suttie, J. Flemming, J.-J. Morcrette, O. Boucher, and M. Schultz, 2009b: Global real-time fire emission estimates based on space-borne fire radiative power observations. *AIP Conference Proceedings*, Vol. 1100, 645.

Knote, C., et al., 2011: Towards an online-coupled chemistry-climate model: evaluation of trace gases and aerosols in COSMO-ART. *Geosci. Model Dev.*, **4 (4)**, 1077–1102, doi:10.5194/gmd-4-1077-2011.

Konovalov, I., M. Beekmann, I. Kuznetsova, A. Yurova, and A. Zvyagintsev, 2011: Atmospheric impacts of the 2010 Russian wildfires: integrating modelling and measurements of an extreme air pollution episode in the Moscow region. *Atmos. Chem. Phys.*, **11 (19)**, 10 031–10 056, doi:10.5194/acp-11-10031-2011.

Koren, I., Y. J. Kaufman, L. A. Remer, and J. V. Martins, 2004: Measurement of the Effect of Amazon Smoke on Inhibition of Cloud Formation. *Science*, **303 (5662)**, 1342–1345, doi:10.1126/science.1089424.

Liu, Z., et al., 2009: The calipso lidar cloud and aerosol discrimination: version 2 algorithm and initial assessment of performance. *J. Atmos. Ocean. Tech.*, **26 (7)**, 1198–1213, doi:10.1175/2009JTECHA1229.1.

Lohmann, U. and J. Feichter, 2001: Can the direct and semi-direct aerosol effect compete with the indirect effect on a global scale? *Geophys. Res. Lett.*, **28 (1)**, 159–161, doi:10.1029/2000GL012051.

Luderer, G., J. Trentmann, T. Winterrath, C. Textor, M. Herzog, H. F. Graf, and M. O. Andreae, 2006: Modeling of biomass smoke injection into the lower stratosphere by a large forest fire (Part II): Sensitivity studies. *Atmos. Chem. Phys.*, **6 (12)**, 5261–5277.

Lundgren, K., B. Vogel, H. Vogel, and C. Kottmeier, 2013: Direct radiative effects of sea salt for the Mediterranean region under conditions of low to moderate wind speeds. *J. Geophys. Res.-Atmos.*, **118 (4)**, 1906–1923, doi:10.1029/2012JD018629.

Majewski, D., et al., 2002: The operational global icosahedral-hexagonal gridpoint model GME: Description and high-resolution tests. *Mon. Weather Rev.*, **130 (2)**, 319–338.

McRae, D. J., J.-Z. Jin, S. G. Conard, A. I. Sukhinin, G. A. Ivanova, and T. W. Blake, 2005: Infrared characterization of fine-scale variability in behavior of boreal forest fires. *Can. J. Forest Res.*, **35 (9)**, 2194–2206, doi:10.1139/x05-096.

Mu, M., et al., 2011: Daily and 3-hourly variability in global fire emissions and consequences for atmospheric model predictions of carbon monoxide. *J. Geophys. Res.-Atmos.*, **116 (D24)**, doi:10.1029/2011JD016245, d24303.

Omar, A., D. Winker, M. Vaughan, Y. Hu, C. Trepte, R. Ferrare, K.-P. Lee, and C. Hostetler, 2009: The CALIPSO Automated Aerosol Classification and Lidar Ratio Selection Algorithm. *J. Atmos. Ocean. Tech.*, **26 (10)**, 1994–2014, doi:10.1175/2009JTECHA1231.1.

Penner, J. E., L. H. Jr, and L. L. Edwards, 1986: Smoke-plume distributions above large-scale fires: Implications for simulations of "nuclear winter". *J. Appl. Meteorol.*, **25 (10)**, 1434–1444, doi:10.1175/1520-0450(1986)025<1434:SPDALS>2.0.CO;2.

Pfister, G., et al., 2005: Quantifying CO emissions from the 2004 Alaskan wildfires using MOPITT CO data. *Geophys. Res. Lett.*, **32 (11)**, doi:10.1029/2005GL022995, l11809.

Prins, E. M., J. M. Feltz, W. P. Menzel, and D. E. Ward, 1998: An overview of GOES-8 diurnal fire and smoke results for SCAR-B and 1995 fire season in South America. *J. Geophys. Res.-Atmos.*, **103 (D24)**, 31 821–31 835, doi:10.1029/98JD01720.

Rieger, D., M. Bangert, C. Kottmeier, H. Vogel, and B. Vogel, 2014: Impact of aerosol on post-frontal convective clouds over Germany. *Tellus B*, **66 (0)**, doi:10.3402/tellusb.v66.22528.

Riemer, N., H. Vogel, B. Vogel, and F. Fiedler, 2003: Modeling aerosols on the mesoscale-γ: Treatment of soot aerosol and its radiative effects. *J. Geophys. Res.-Atmos.*, **108 (D19)**, doi:10.1029/2003JD003448, 4601.

Sakamoto, K., J. Allan, H. Coe, J. Taylor, T. Duck, and J. Pierce, 2015: Aged boreal biomass-burning aerosol size distributions from bortas 2011. *Atmos. Chem. Phys.*, **15 (4)**, 1633–1646, doi:10.5194/acp-15-1633-2015.

Sessions, W. R., H. E. Fuelberg, R. A. Kahn, and D. M. Winker, 2011: An investigation of methods for injecting emissions from boreal wildfires using WRF-Chem during ARCTAS. *Atmos. Chem. Phys.*, **11 (12)**, 5719–5744, doi:10.5194/acp-11-5719-2011.

Sofiev, M., T. Ermakova, and R. Vankevich, 2012: Evaluation of the smoke-injection height from wild-land fires using remote-sensing data. *Atmos. Chem. Phys.*, **12 (4)**, 1995–2006, doi:10.5194/acp-12-1995-2012.

Stanelle, T., B. Vogel, H. Vogel, D. Bäumer, and C. Kottmeier, 2010: Feedback between dust particles and atmospheric processes over West Africa during dust episodes in March 2006 and June 2007. *Atmos. Chem. Phys.*, **10 (22)**, 10 771–10 788, doi:10.5194/acp-10-10771-2010.

Stocker, T., et al., 2013: IPCC, 2013: Climate Change 2013: The Physical Science Basis. Contribution of Working Group I to the Fifth Assessment Report of the Intergovernmental Panel on Climate Change. Cambridge University Press, Cambridge, United Kingdom and New York, NY, USA.

Tosca, M. G., J. T. Randerson, C. S. Zender, D. L. Nelson, D. J. Diner, and J. A. Logan, 2011: Dynamics of fire plumes and smoke clouds associated with peat and deforestation fires in Indonesia. *J. Geophys. Res.-Atmos.*, **116 (D8)**, doi:10.1029/2010JD015148, d08207.

Trentmann, J., M. O. Andreae, H.-F. Graf, P. V. Hobbs, R. D. Ottmar, and T. Trautmann, 2002: Simulation of a biomass-burning plume: Comparison of model results with observations. *J. Geophys. Res.-Atmos.*, **107 (D2)**, doi:10.1029/2001JD000410.

Trentmann, J., et al., 2006: Modeling of biomass smoke injection into the lower stratosphere by a large forest fire (Part I): reference simulation. *Atmos. Chem. Phys.*, **6 (12)**, 5247–5260, doi:10.5194/acp-6-5247-2006.

Tummon, F., F. Solmon, C. Liousse, and M. Tadross, 2010: Simulation of the direct and semidirect aerosol effects on the southern Africa regional climate during the biomass burning season. *J. Geophys. Res.-Atmos.*, **115 (D19)**, doi:10.1029/2009JD013738, d19206.

Val Martin, M., J. A. Logan, R. A. Kahn, F. Leung, D. L. Nelson, and D. J. Diner, 2010: Smoke injection heights from fires in North America: analysis of 5 years of satellite observations. *Atmos. Chem. Phys.*, **10 (4)**, 1491–1510.

Vogel, B., H. Vogel, D. Bäumer, M. Bangert, K. Lundgren, R. Rinke, and T. Stanelle, 2009: The comprehensive model system COSMO-ART – Radiative impact of aerosol on the state of the atmosphere on the regional scale. *Atmos. Chem. Phys.*, **9 (22)**, 8661–8680, doi:10.5194/acp-9-8661-2009.

Vogel, H., J. Förstner, B. Vogel, T. Hanisch, B. Mühr, U. Schättler, and T. Schad, 2014: Time-lagged ensemble simulations of the dispersion of the Eyjafjallajökull plume over Europe with COSMO-ART. *Atmos. Chem. Phys.*, **14 (15)**, 7837–7845, doi:10.5194/acp-14-7837-2014.

Waibel, A., H. Fischer, F. Wienhold, P. Siegmund, B. Lee, J. Ström, J. Lelieveld, and P. Crutzen, 1999: Highly elevated carbon monoxide concentrations in the upper troposphere and lowermost stratosphere at northern midlatitudes during the STREAM II summer campaign in 1994. *Chemosphere - Global Change Science*, **1 (1)**, 233–248, doi:10.1016/S1465-9972(99)00027-6.

Wang, J., S. A. Christopher, U. S. Nair, J. S. Reid, E. M. Prins, J. Szykman, and J. L. Hand, 2006: Mesoscale modeling of Central American smoke transport to the United States: 1."Top-down" assessment of emission strength and diurnal variation impacts. *J. Geophys. Res.-Atmos.*, **111 (D5)**, doi:10.1029/2005JD006416, d05S17.

Wang, J., et al., 2013: Mesoscale modeling of smoke transport over the Southeast Asian Maritime Continent: interplay of sea breeze, trade wind, typhoon, and topography. *Atmos. Res.*, **122**, 486–503, doi:10.1016/j.atmosres.2012.05.009.

Wiedinmyer, C., S. Akagi, R. Yokelson, L. Emmons, J. Al-Saadi, J. Orlando, and A. Soja, 2011: The Fire INventory from NCAR (FINN): A high resolution global model to estimate the emissions from open burning. *Geosci. Model Dev.*, **4 (3)**, 625–641, doi:10.5194/gmd-4-625-2011.

Wooster, M. J., G. Roberts, G. L. W. Perry, and Y. J. Kaufman, 2005: Retrieval of biomass combustion rates and totals from fire radiative power observations: FRP derivation and calibration relationships between biomass consumption and fire radiative energy release. *J. Geophys. Res.-Atmos.*, **110 (D24)**, doi:10.1029/2005JD006318, d24311.

Zhang, X. and S. Kondragunta, 2008: Temporal and spatial variability in biomass burned areas across the USA derived from the GOES fire product. *Remote Sens. Environ.*, **112 (6)**, 2886–2897, doi:10.1016/j.rse.2008.02.006.

Zhang, X., S. Kondragunta, J. Ram, C. Schmidt, and H.-C. Huang, 2012: Near-real-time global biomass burning emissions product from geostationary satellite constellation. *J. Geophys. Res.-Atmos.*, **117 (D14)**, doi:10.1029/2012JD017459, d14201.

Atmos. Chem. Phys. Discuss., doi:10.5194/acp-2015-964, 2016
Manuscript under review for journal Atmos. Chem. Phys.
Published: 19 January 2016

Atmospheric Chemistry and Physics Discussions

Table 1. Chemical composition, number-median diameter, and standard deviation of the lognormal distributions of the eight modes. (NUC: nucleation mode, NUCS: nucleation mode containing a soot core, ACC: accumulation mode, ACCS: accumulation mode containing a soot core, SOOT: pure soot mode, SEASA: sea salt fine, SEASB: sea salt medium, SEASC: sea salt coarse)

	NUC	NUCS	ACC	ACCS	SOOT	SEASA	SEASB	SEASC
soot		•		•	•			
sulfate	•	•	•	•		•	•	•
ammonium	•	•	•	•				
nitrate	•	•	•	•				
organics	•	•	•	•				
water	•	•	•	•		•	•	•
sodium chloride						•	•	•
	Initial diameter in μm							
	0.01	0.08	0.07	0.08	0.08	0.2	2	12
	Standard deviation							
	1.7	1.7	2.0	2.0	1.4	1.9	2.0	1.7

Table 2. Specification of the realised simulations

	diurnal cycle fire intensity & size	diurnal cycle emission strength	vert. dist. profile	homogeneous vert. dist.
VARHEIGHT	•		•	
EMISSCYCLE	•	•	•	
800M				•
7500M				•
NOFIRE				

Atmos. Chem. Phys. Discuss., doi:10.5194/acp-2015-964, 2016
Manuscript under review for journal Atmos. Chem. Phys.
Published: 19 January 2016

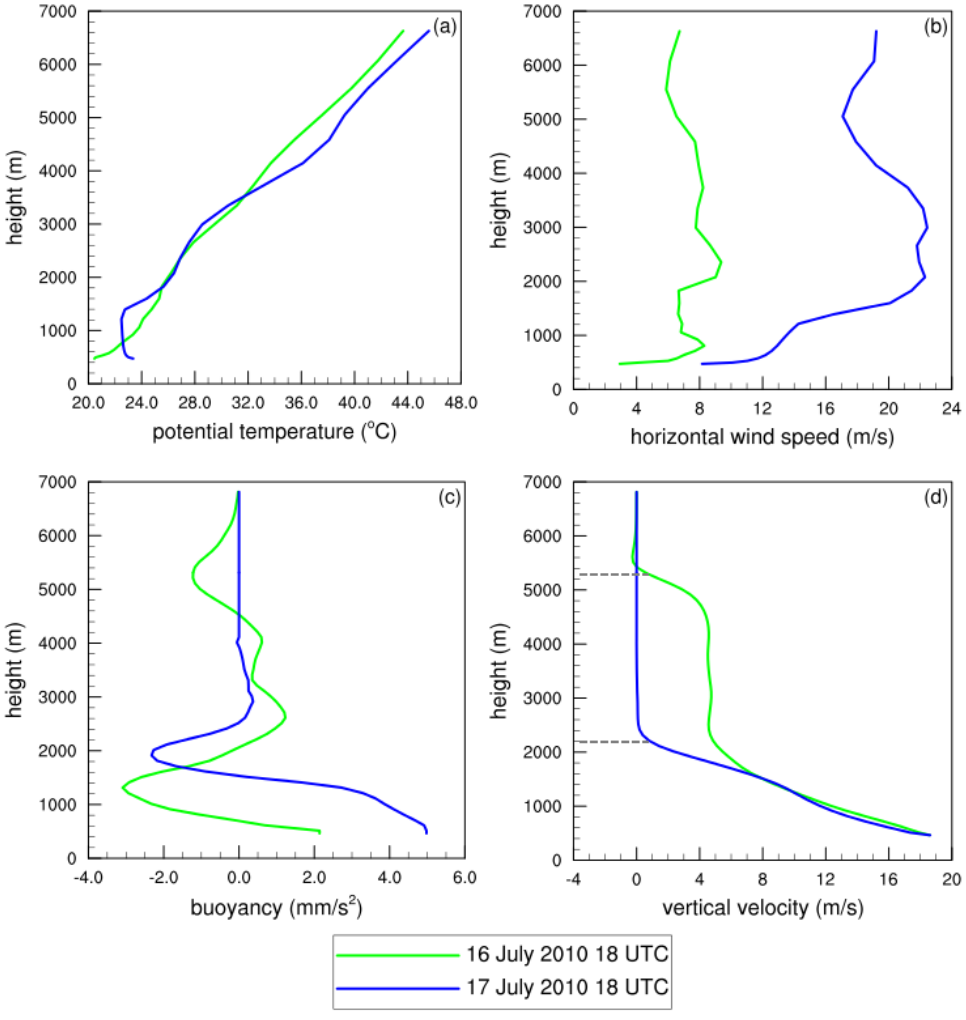

Figure 1. The potential temperature (a) and horizontal wind speed (b) of the environment and the calculated buoyancy (c) and vertical velocity (d) for an imaginary fire in central Saskatchewan, Canada, for 16 July 2010 at 1800 UTC and 17 July 2010 at 1800 UTC.

Atmos. Chem. Phys. Discuss., doi:10.5194/acp-2015-964, 2016
Manuscript under review for journal Atmos. Chem. Phys.
Published: 19 January 2016

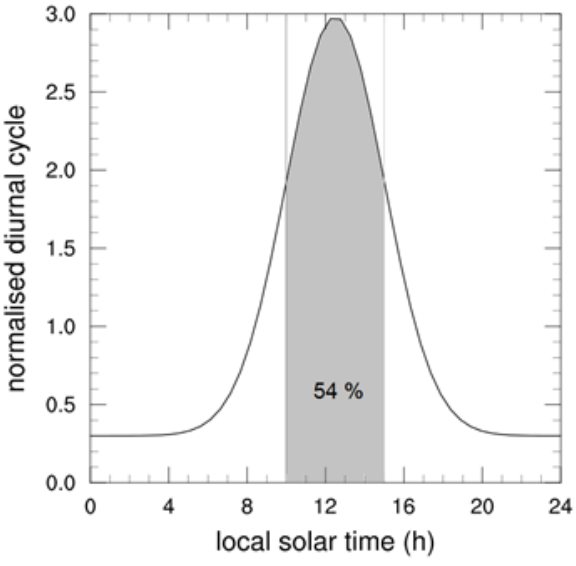

Figure 2. The course of the diurnal cycle for boreal forests.

Atmos. Chem. Phys. Discuss., doi:10.5194/acp-2015-964, 2016
Manuscript under review for journal Atmos. Chem. Phys.
Published: 19 January 2016

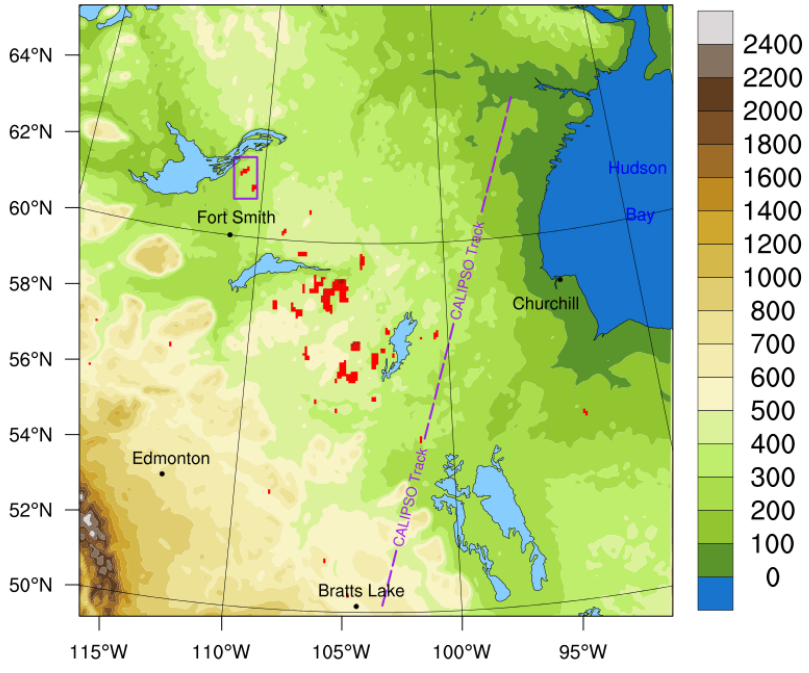

Figure 3. Simulation domain with model orography without the relaxation area. The fire locations are marked in red for 15 July 2014. The CALIPSO overpass at around 0920 UTC 16 July 2010 is denoted by a purple line. The area near Fort Smith framed with a purple line is used to characterize the aerosol size distribution.

Atmos. Chem. Phys. Discuss., doi:10.5194/acp-2015-964, 2016
Manuscript under review for journal Atmos. Chem. Phys.
Published: 19 January 2016

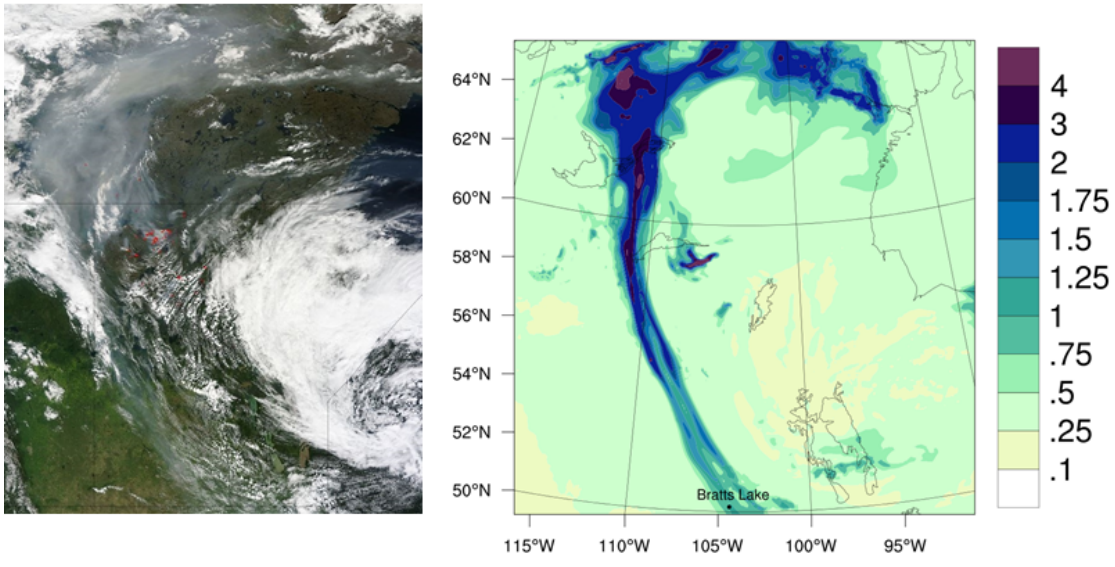

Figure 4. Left: Satellite image in the visible section at 1755 UTC 15 July 2010. The center of the image is located at 56° N and 102° E (LANCE Rapid Response MODIS Image Gallery, NASA). Right: Simulated aerosol optical depth at 1800 UTC 15 July 2010.

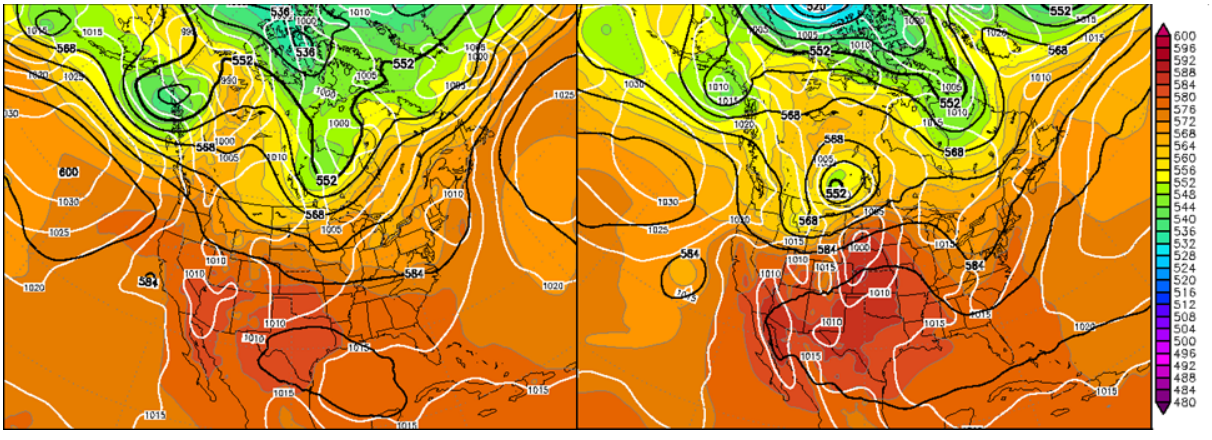

Figure 5. Reanalysis (Climate Forecast System, CFS) of the meteorological conditions on 11 July 2010 at 1800 UTC (left) and 14 July 2010 at 0600 UTC (right), 500 hPa geopotential (gpdm) black lines, surface pressure (hPa) white lines and relative topography H500-H1000 (gpdm) colour coding (www.wetter3.de).

Atmos. Chem. Phys. Discuss., doi:10.5194/acp-2015-964, 2016
Manuscript under review for journal Atmos. Chem. Phys.
Published: 19 January 2016

Atmospheric Chemistry and Physics Discussions

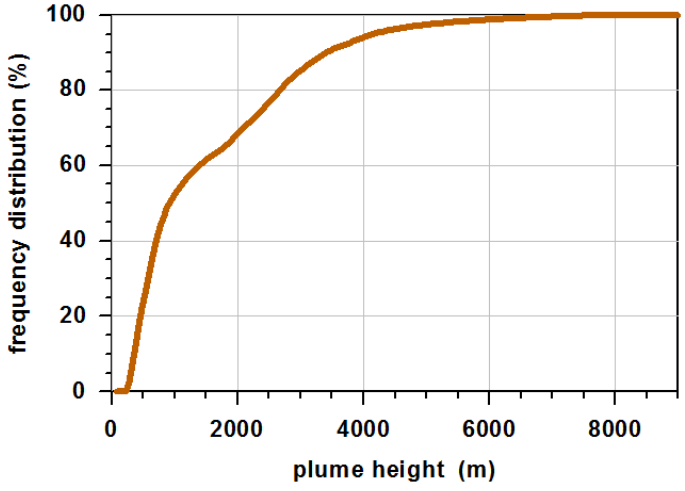

Figure 6. Accumulated frequency distribution of the simulated plume heights for the ten day time period from 10 July 2010 to 20 July 2010. In total 52628 data points are included.

Atmos. Chem. Phys. Discuss., doi:10.5194/acp-2015-964, 2016
Manuscript under review for journal Atmos. Chem. Phys.
Published: 19 January 2016

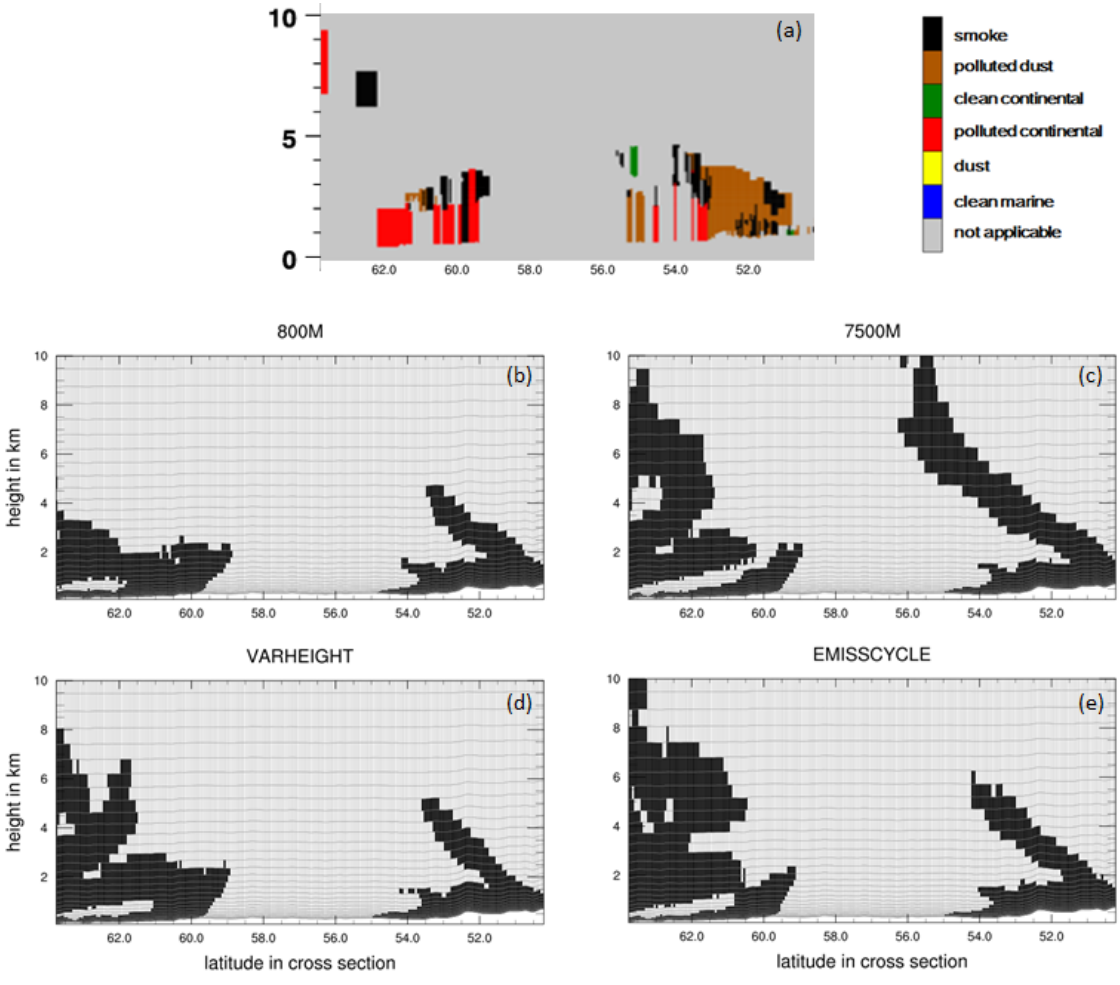

Figure 7. Cross section of aerosol subtypes of CALIPSO overpass at around 0920 UTC 16 July 2010 (a). Cross section along the same CALIPSO track for simulations 800M (b), 7500M (c), VARHEIGHT (d) and EMISSCYCLE (e), here only soot is displayed.

Atmos. Chem. Phys. Discuss., doi:10.5194/acp-2015-964, 2016
Manuscript under review for journal Atmos. Chem. Phys.
Published: 19 January 2016

Atmospheric Chemistry and Physics Discussions

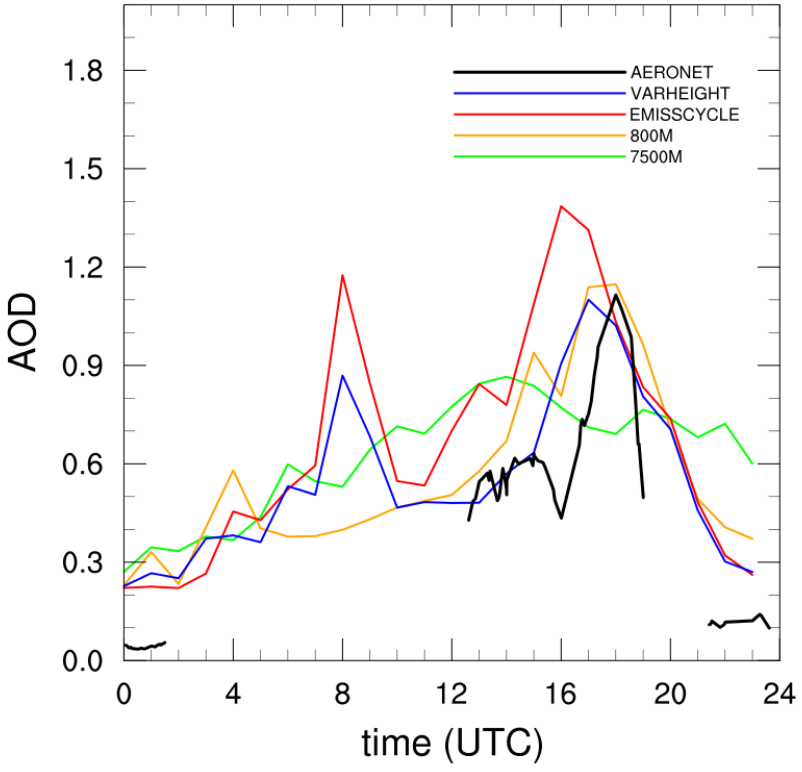

Figure 8. Comparison of measured (AERONET) and simulated AOD at Bratts Lake for 15 July 2010.

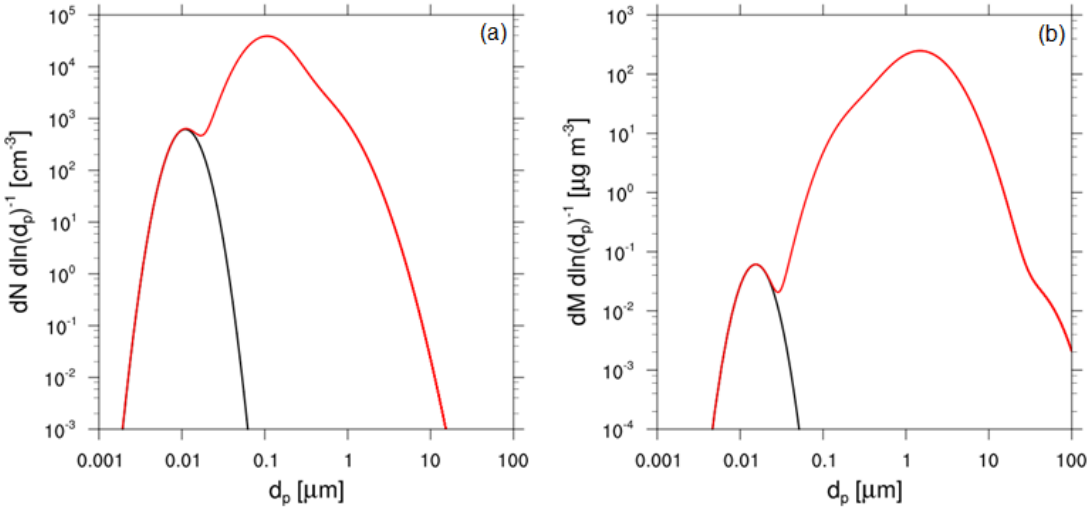

Figure 9. Number size distribution (a) and mass size distribution (b) for soot (black) and the sum of all modes (red).

Atmos. Chem. Phys. Discuss., doi:10.5194/acp-2015-964, 2016
Manuscript under review for journal Atmos. Chem. Phys.
Published: 19 January 2016

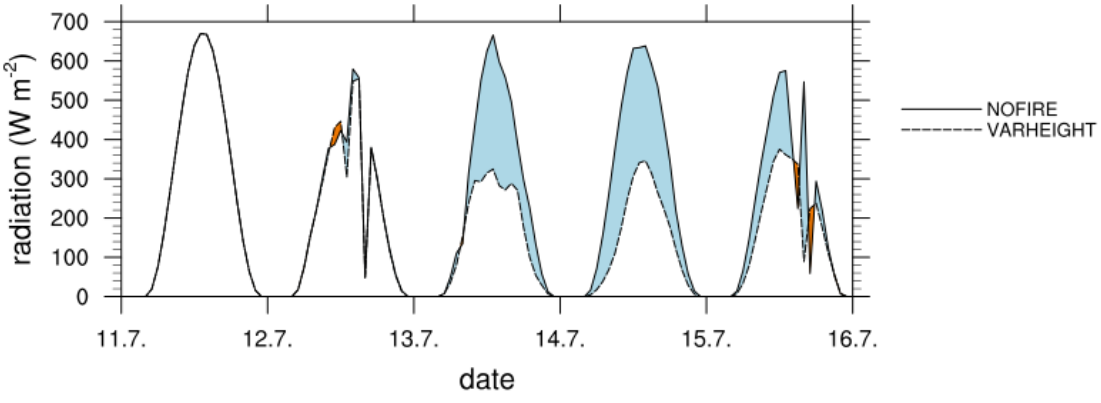

Figure 10. Surface short-wave radiation in Fort Smith for five days starting on 11 July 2010.

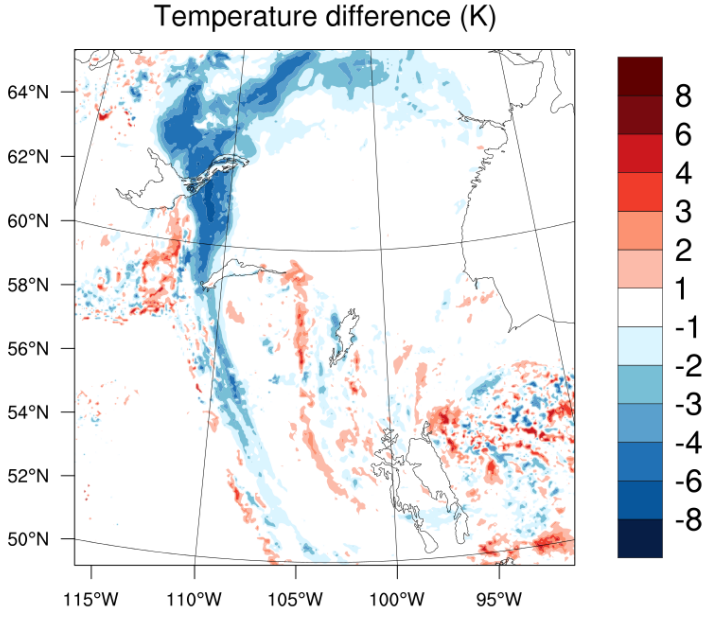

Figure 11. Temperature changes in 2 m height at 1800 UTC 15 July 2010. Displayed is the difference between the simulations VARHEIGHT and NOFIRE.

Atmos. Chem. Phys. Discuss., doi:10.5194/acp-2015-964, 2016
Manuscript under review for journal Atmos. Chem. Phys.
Published: 19 January 2016

Atmospheric Chemistry and Physics Discussions

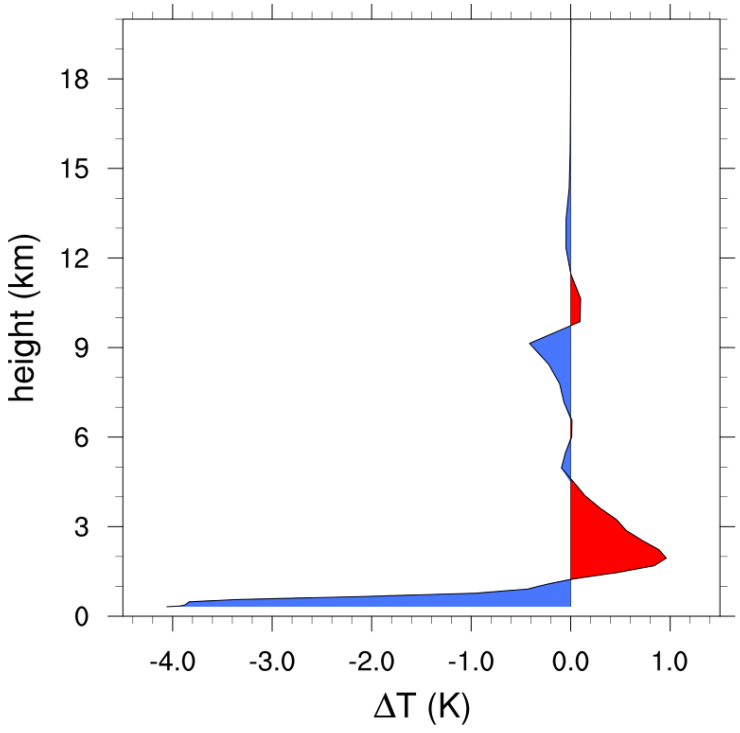

Figure 12. Mean vertical temperature change between the simulations VARHEIGHT and NOFIRE for a small domain around Fort Smith for 1800 UTC 15 July 2010.

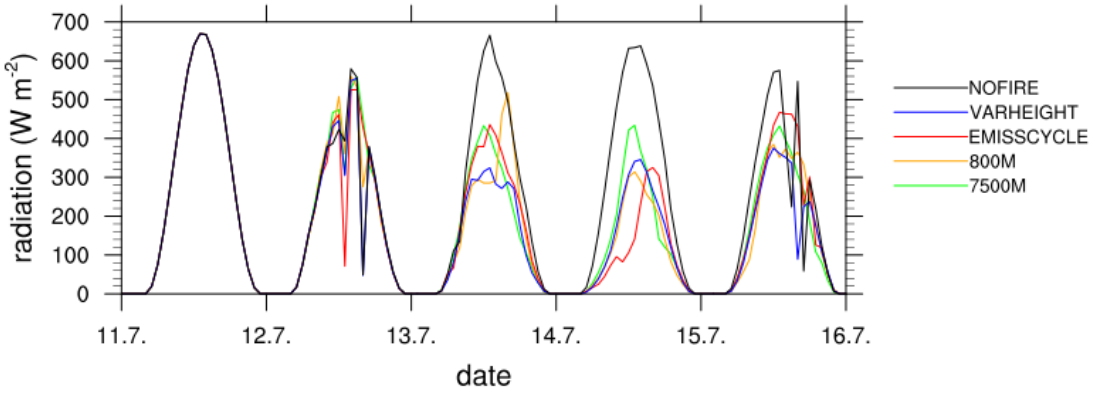

Figure 13. Surface short-wave radiation at Fort Smith for five days starting on 11 July 2010 for the different simulations.